

Department of Physics and Astronomy
University of Heidelberg

Bachelor Thesis in Physics
submitted by

Lukas Renner

born in Düsseldorf (Germany)

2013

Angular Correlations in Proton-Lead Collisions at the LHCb-Experiment

This Bachelor Thesis has been carried out by Lukas Renner at the
Physikalisches Institut in Heidelberg
under the supervision of
Prof. Dr. Ulrich Uwer

Abstract

In this thesis, angular correlations of particles produced in proton-lead collisions are investigated by calculating two-particle correlation functions. A data set of 25 million events, at a center-of-mass-energy per nucleon pair of 5 TeV, collected with the LHCb detector in 2013, is used to perform the analysis. Measuring particle correlations gives an insight into the production mechanism of particles and possible emerging effects due to interaction of the partonic matter. Of particular interest is a ridge-like structure, appearing at a relative azimuthal angle of zero in the correlation function of high multiplicity collisions. This "near-side" ridge structure has been observed for the first time in the kinematic forward region. A qualitative study of its properties compares to the results obtained in the central rapidity region.

Kurzfassung

In dieser Arbeit werden, mit Hilfe von Zwei-Teilchen Korrelationsfunktionen, die Winkelkorrelationen von Teilchen untersucht, die in Proton-Blei Kollisionen erzeugt wurden. Es wird ein 25 Millionen Ereignisse umfassender Datensatz verwendet, der 2013 mit dem LHCb Detektor aufgenommen wurde. Die Schwerpunktsenergie pro Nukleonpaar beträgt $\sqrt{s_{NN}} = 5$ TeV. Die Analyse von Teilchenkorrelationen ermöglicht einen Einblick in den Produktionsmechanismus der Teilchen, sowie in zusätzliche Effekte, bedingt durch Interaktionen der Teilchen. Von besonderem Interesse ist eine Korrelationsstruktur, die bei einem relativen Azimutalwinkel von 0 in Kollisionen mit hoher Multiplizität auftritt. Diese Struktur wurde zum ersten Mal in der kinematischen Vorwärtsrichtung beobachtet. Eine qualitative Untersuchung ihrer Eigenschaften zeigt eine Übereinstimmung mit Ergebnissen, die im zentralen Rapiditätsbereich erzielt wurden.

Contents

1	Introduction	7
2	The two-particle angular correlation function	9
3	The LHCb detector	11
3.1	The Vertex Locator	11
3.2	The RICH detectors	11
3.3	The Magnet	13
3.4	The tracking system	13
3.5	The calorimeters	13
3.6	The muon system	14
4	Data sets	15
4.1	Event selection	15
4.2	Track selection	17
5	Determination of the two-particle angular correlation function	23
6	Corrections for tracking-efficiency, acceptance and ghostfraction	27
6.1	Determination of the corrections	27
6.2	Consistency check and influence of binning	33
7	Results	39
8	Conclusion	43

1 Introduction

Proton-ion and proton-proton collisions at high energies provide the possibility to investigate the behaviour of nuclear matter, predicted by Quantum Chromodynamics. In these collisions extreme temperatures and particle densities are reached, enabling the study of particle production mechanisms, especially hadronization, as well as possible emerging effects due to the high densities. Previous studies have investigated this, by using multi-particle correlations [6–10]. By measuring the differences in the polar angle ϕ and the pseudo-rapidity $\eta = -\ln(\tan(\theta/2))$, where θ is the azimuthal angle, measured with respect to the beam axis, a two-particle correlation-function $C(\Delta\eta, \Delta\phi)$ is constructed, whose shape depends on a multitude of quantities, such as the event-multiplicity or the transverse momentum of the considered particles. This method was first used to analyse collisions of large nuclei, to investigate the formation of dense partonic matter. Recently several studies employing this technique in proton-proton and proton-ion collisions have been carried out, among others by the ALICE- and CMS-collaborations at the LHC [15–17]. A certain ridge-like structure in the correlation-function also present in ion-ion collisions is of particular interest. In ion-ion collisions, theories are able to predict its appearance and its shape [1–5], but these explanations cannot be applied to proton-proton or proton-ion collisions, because the particle densities are too low. Investigations concerning this subject at LHCb are particularly interesting because the LHCb detector covers a range of pseudo-rapidity (from 2.0 to 4.8), which tests the kinematic forward range, that cannot be accessed by central rapidity detectors.

2 The two-particle angular correlation function

Figure 2.1 shows an example of a two-particle angular correlation histogram. It is obtained by forming pairs of particles. The angular differences $\Delta\eta = |\eta_1 - \eta_2|$ and $\Delta\phi = |\phi_1 - \phi_2|$ of these pairs are measured and filled into a two-dimensional histogram with bins of $\Delta\eta$ and $\Delta\phi$, so that each pair generates one entry in the histogram. A high correlation in a bin is then indicated by a large number of entries the bin. The most prominent feature is the so called “near-side peak” around $\Delta\eta = \Delta\phi = 0$. This peak is related to particles in jets and high p_T clusters. These particles move close to each other, so pairs consisting of these particles will have small angular differences. If clusters have a low transverse momentum they will travel close to the beam axis (at small pseudo-rapidities), or around it, distributed over the whole range of ϕ . This is the reason a ridge-like structure at $\Delta\eta \approx 0$, spanning the whole $\Delta\phi$ range can be observed. Another important contribution to the correlation function is the “away-side ridge” at $\Delta\phi = \pi$. It is caused by “back-to-back jets” (regarding the azimuthal angle). Momentum conservation leads to a difference in the polar angle of π . Because these jets may consist of particles with different masses, their particles are spread over a wide range of $\Delta\eta$ without violating momentum conservation, resulting in a ridge that is elongated in $\Delta\eta$. Of particular interest is an additional long-range (large $\Delta\eta$), ridge-like structure, that becomes visible only in high-multiplicity collisions. It lies at $\Delta\phi = 0$ and is most pronounced in an intermediate range of transverse momentum. This ridge has first been observed in $AuAu$ collisions at the Relativistic Heavy Ion Collider (RHIC) [10]. In the case of ion-ion collisions there are plausible explanations for this structure [11–14], but is also present in pp collisions where these explanations are not valid. The pPb collisions analyzed here offer another possibility to study this subject. Various theories explaining the emergence of this ridge exist (reference), but a definite answer is yet to be found.

$1 \text{ GeV} \leq p_{\perp} < 2 \text{ GeV}$
 $0 \leq N_{sl} < 10$

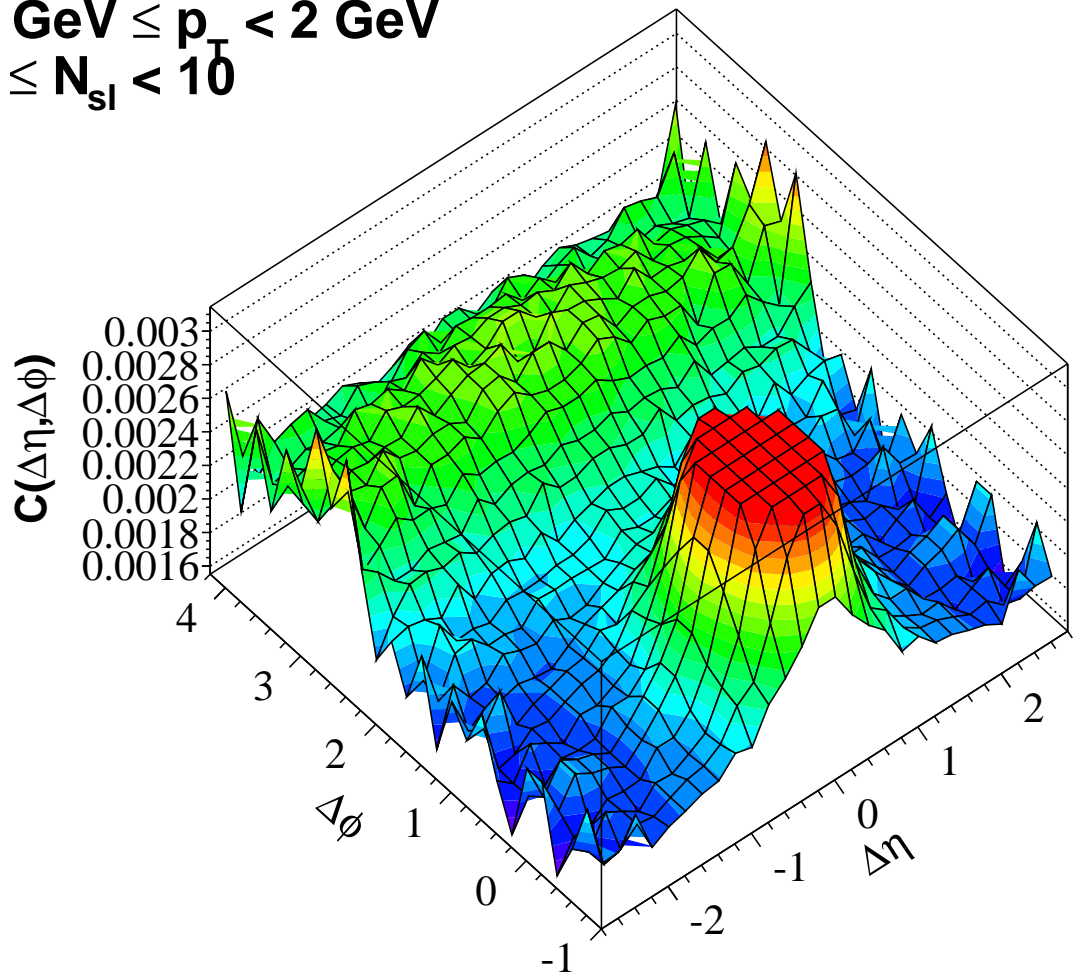


Figure 2.1: An Example of a correlation function

3 The LHCb detector

The LHCb detectors primary task is to measure b- and c-hadron decays. Because these particles are mainly produced in the forward direction, close to the beam axis, the detector differs significantly from the other detectors at LHC. Its components are arranged around the beam axis and are thus able to detect particles with high rapidities ranging from $\Delta\eta = 2.0$ to $\Delta\eta = 4.8$. The detector is built as a single-arm forward spectator and can only detect particles on one side of the collision. The coordinate system used is a right-handed one, where the z-axis is identical with the beam axis, so that detectable particles have positive z-positions. The y-axis is chosen horizontally, hence the x-axis reaches upwards. The main components are the Vertex Locator (VELO), the RICH detectors, the magnet, the tracking stations, the calorimeter and the muon system. They are shown in figure 3.1 and will be briefly presented in the following.

3.1 The Vertex Locator

The VELO is placed upstream (before the magnet), surrounding the collision point. It consists of 42 semi-circular silicon strip detectors, that are positioned on either side of the beam-axis. While the beam is not focused, these semi-circles are moved to the side, to a distance of 35 mm, so they may not be directly hit by the beam. When taking data, they are moved inwards, approximately 7 mm away from the beam. When a charged particles moves through one of the silicon-detectors, electron-hole pairs are created. Their position can be located, and in turn the particles track trough the VELO can be reconstructed.

3.2 The RICH detectors

The two “ring imaging Cherenkov” (RICH) detectors are positioned before and after the magnet. They are used to identify charged hadrons, by detecting Cherenkov radiation.

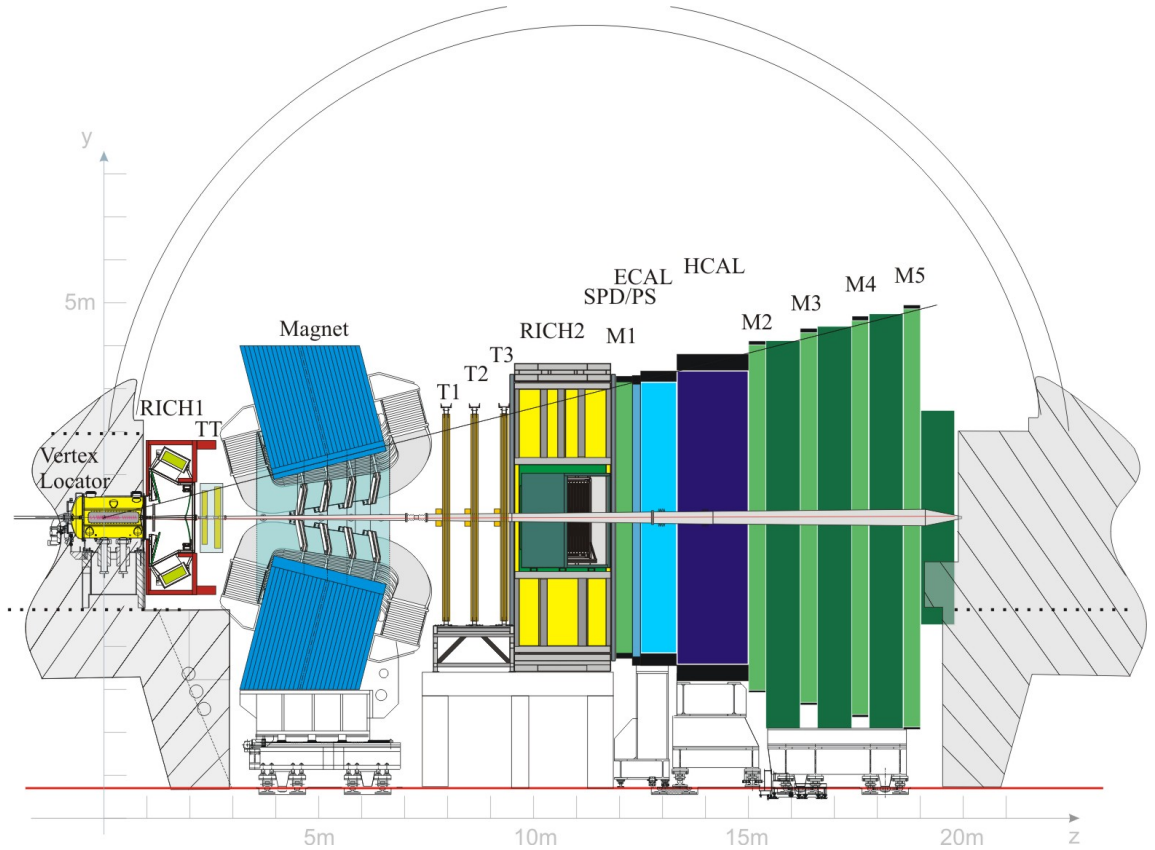


Figure 3.1: The LHCb detector

By measuring the angle of emission θ_c of the radiation it is possible to determine the particles velocity: $\beta = \frac{1}{n \cdot \cos\theta_c}$, given the refractive index of the medium. The first one (RICH-1), positioned directly behind the VELO, uses silica aerogel and C_4F_{10} gas to detect particles over a momentum range of 1-65 GeV. The RICH-2 detector is placed behind the magnet and is designed to detect particles with momenta from 15 GeV up to 150 GeV. It is filled with CF_4 gas that works as a radiator, and its acceptance is limited to small angles close to the beam axis. In both detectors, spherical mirrors direct the Cherenkov photons on hybrid photon detectors (HPDs). Each of them contains a photocathode, in which the Cherenkov photons are converted to photo electrons. The electrons then in turn travel through a vacuum on to a silicon detector, where they create electron-hole pairs. The position of these electron-hole pairs can be measured using read-out electronics.

3.3 The Magnet

In order to identify particles, it is necessary to know their momentum. In the LHCb detector a dipole magnet leads to a curvature of the trajectories of all charged particles flying through its field depending on the particle's momentum. Because of the high particle momenta (up to 200 GeV), an integrated magnetic field of 4 T m is required.

3.4 The tracking system

The first part of the tracking system comprises the “Trigger Tracker” (TT) which is located between RICH-1 and the magnet. It consists of silicon strip detectors, in which an electric charge is created when a particle traverses it. The position where the particle crossed the detector can be determined by locating the electric charge. There are three more tracking stations, each consisting of two parts. The first part, the “Inner Tracker” (IT) forms a cross-shaped silicon strip detector surrounding the beam-axis. The outer part of the rectangular tracking stations, the “Outer Tracker” (OT), consists of gas filled tubes. The gas inside (70% argon, 30%CO₂) is ionized by passing particles. The emerging electrons are collected at an anode in the middle of the tube, leading to an electric signal that is read out. The position of the traversing track is measured by the drift time of the electrons.

3.5 The calorimeters

Two different calorimeters facilitate the measurement of particle energies: The electromagnetic calorimeter is used for particles interacting mainly via the electromagnetic interaction, i.e. e , γ , whereas the hadronic calorimeter determines the energy of particles interacting via the strong interaction. Both calorimeters function according to the same principle: Incoming particles hit layers of metal, interact and thus create particle showers. Each layer of metal is followed by a layer of plastic. The molecules in these layers are excited by the particle showers and thus emit light that is transmitted through fibers and then read out. The signal is proportional to the energy of the particle.

3.6 The muon system

The five muon stations are placed at the end of the detector, furthest away from the interaction point, because it is unlikely for any particle but a muon to travel that far. Every muon station is composed of multiwire proportional chambers filled with a mixture of argon, CO_2 , and CF_4 , whose interaction with the muons creates electrons drift to wire electrodes, due to an electric field. The induced signal is then read out. The muon system is used to reconstruct the muon tracks, but also for muon identification.

4 Data sets

In general two configurations of proton-lead collisions can be studied. In $Pb p$ collisions lead ions travel in the positive z -direction when traversing the detector, which is also positioned in the positive z -direction, while protons travel in the opposite direction. Accordingly pPb collisions feature lead ions travelling in the positive- and protons travelling into the negative z -direction. In both cases the produced particles are boosted in the direction of the lead ions, because of their higher mass. In the following only pPb collisions are studied. Besides the pPb data a Monte-Carlo simulation is used to calculate corrections for detector effects. Because a pPb simulation is not available, pp is used, which is feasible because it is not used to correct for physical effects. The mean number of primary vertices in the pp simulation is 2.5. By using events with multiple reconstructed primary vertices, the multiplicity in the simulated events reaches the multiplicity of the pPb collisions, as can be seen in figure 4.3. Figure 4.1 shows the number of reconstructed primary vertices per event for both data sets. The main portion of pPb collisions contains one reconstructed primary vertex, while the pp simulation also contains events with higher numbers.

4.1 Event selection

In this analyses each event is required to have exactly one reconstructed primary vertex. Furthermore a cut on the z -position of this vertex is performed, in order to suppress events resulting from beam-gas interaction. Beam-gas interactions occur when particles from the beam collide with residual gas near the interaction point. A Gaussian distribution is fitted to the distribution of the z -positions, shown in figure 4.2; the fit-results are shown in table 4.1. The mean z -position of the reconstructed vertices in the data sample lies close to zero, whereas the mean value of the simulation lies approximately 21 mm away, because it was adjusted to match the mean z -position of a pp data set taken in 2012. This difference might lead to a small deviation in the acceptance. The

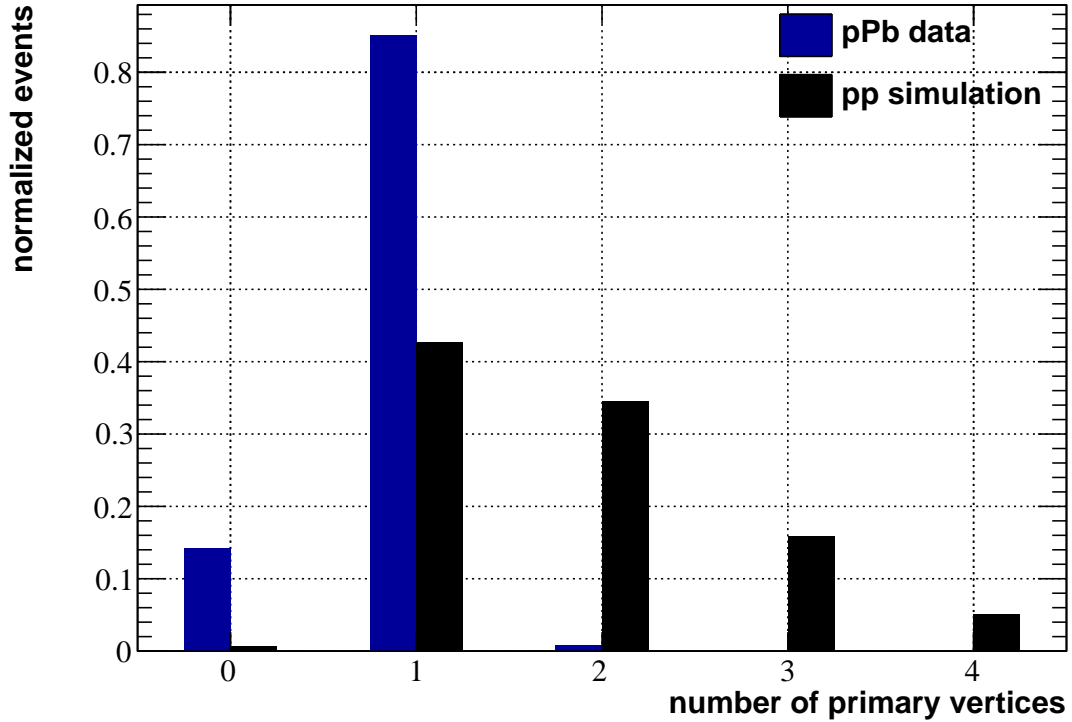


Figure 4.1: number of primary vertices of pPb-data and pp-MC

Table 4.1: Mean z-position and rms of the reconstructed primary vertices

data set	PV mean z-pos. [mm]	rms [mm]
pPb	-0.5458 ± 0.0091	41.7171 ± 0.0057
pp MC	20.2997 ± 0.0145	39.1070 ± 0.0101

primary vertex of the selected events has to lie within 3σ of the fitted mean. However we are only able to exclude those interactions that happen at high distances to the fitted mean, but as these interactions may occur at any position there is always a background remaining. This background can be seen as a flat distribution on both sides, whereas the main peak in the middle is due to the pPb interactions.

Moreover a “minimum-bias trigger” is used in the event selection, requiring every selected event to contain at least one reconstructed track. The data set contains a total of 25 million events, whereof 19 million events remain after the selection.

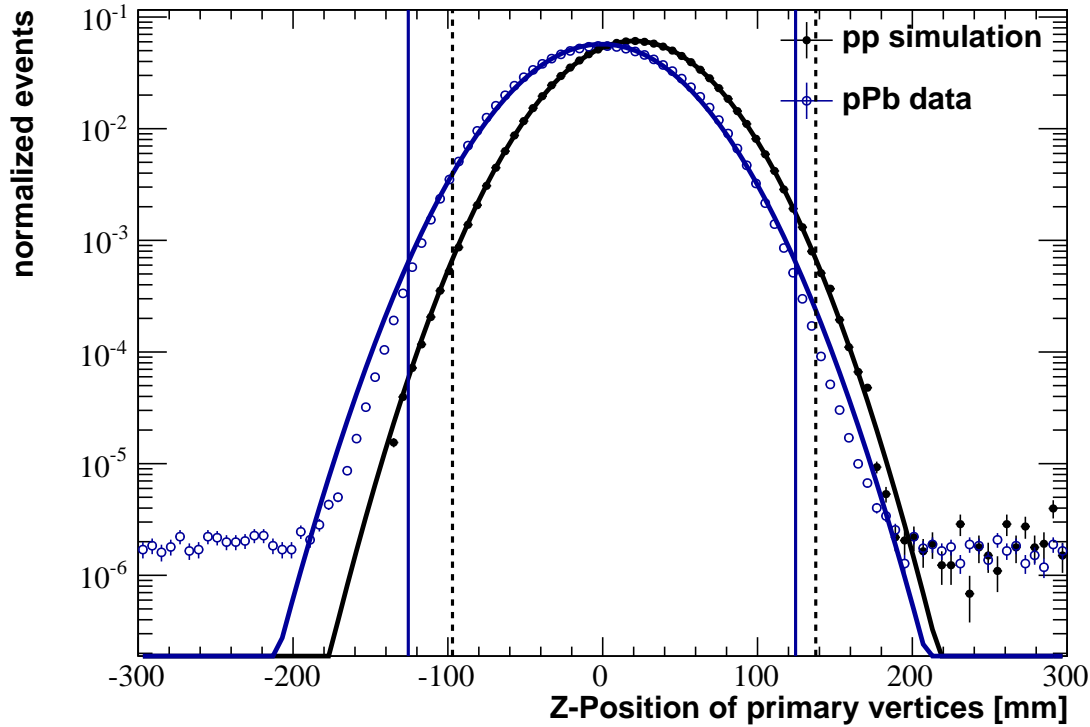


Figure 4.2: Z-positions of the reconstructed primary vertices of pPb-data and the simulation. The lines mark a 3σ difference to the fitted mean (indicated by dashed lines for the simulation).

4.2 Track selection

Only “long tracks” are used to calculate the correlation function, meaning they are required to have hits in the VELO and the T-stations. Furthermore kinematic cuts are applied. Reconstructed tracks have to lie in a pseudo-rapidity range from $\eta = 2.0$ up to $\eta = 4.8$, and must have a momentum $p > 2\text{ GeV}$ and a transverse momentum $p_t > 150\text{ MeV}$, because this is the kinematic region accessible by the detector. Because their angular distributions contain no relevant information, the portion of secondary particles is reduced by a constraint of the impact-parameter: $ip < 0.2\text{ mm}$. Tracks passing these cuts are called selected long tracks.

The analysis is performed in four separate bins of multiplicity, i.e. the number of selected long tracks per event, N_{sl} . The binning scheme is shown in table 4.2. Figure 4.3 shows the multiplicity for data and the simulation with indicated bins.

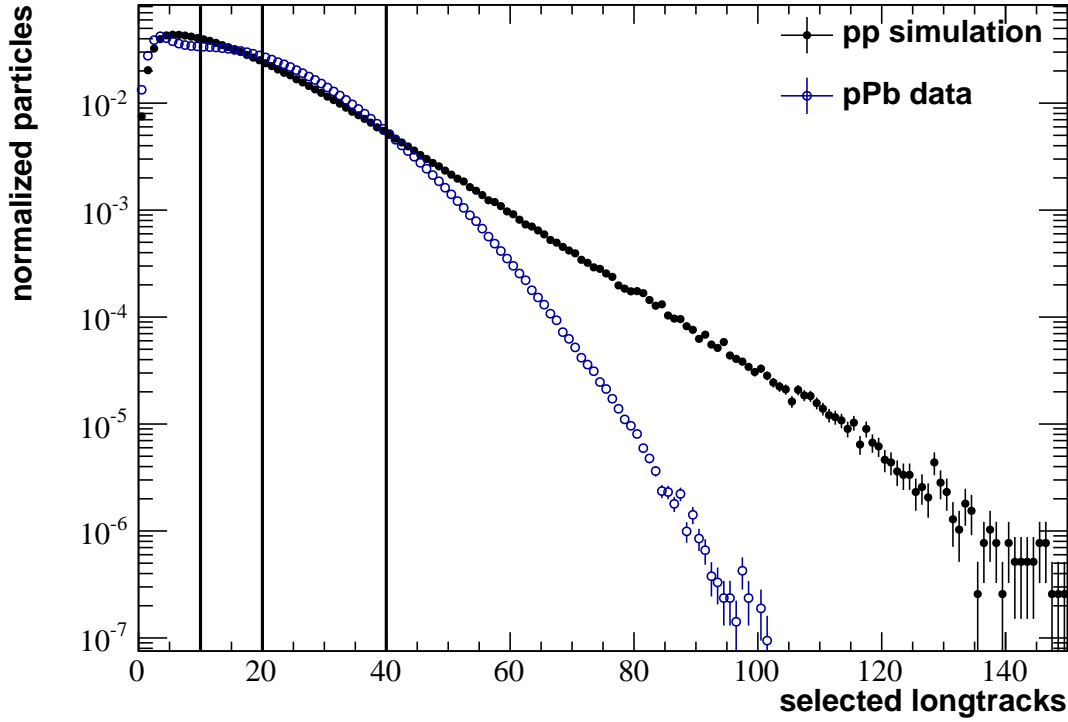


Figure 4.3: Multiplicity distribution of pPb collisions and the pp simulation

Table 4.2: The multiplicity binning scheme

bin	multiplicity	#events	portion [%]	$\langle N_{sl} \rangle$
1	0 – 9	6 436 089	33.80	4.99
2	10 – 19	6 319 068	33.19	14.33
3	20 – 39	5 778 151	30.36	26.72
4	40+	507 806	2.65	44.85

Within each multiplicity bin a correlation histogram is generated using particles within three different ranges of transverse momentum:

- $0.15 \text{ GeV} \leq p_T < 1.00 \text{ GeV}$
- $1.00 \text{ GeV} \leq p_T < 2.00 \text{ GeV}$
- $2.00 \text{ GeV} \leq p_T < 3.00 \text{ GeV}$

The p_T distribution with indicated bins is shown figure 4.4.

The kinematic properties of the selected tracks are shown in figure 4.5. Figure 4.5a shows the distribution of pseudo-rapidity. At $4.2 < \eta < 4.5$ the portion of detected particles decreases significantly, which is due to the shape of the beam pipe. It is thicker in this range, so particles with a corresponding pseudo-rapidity are more likely to interact with the material. Hard-scattering may cause them to leave the detector acceptance, or energy loss in general may prevent them from being detected. A similar effect occurs at certain polar angles, as can be seen in figure 4.5b. The VELO consists of semi-circular discs that overlap around $\phi = \frac{\pi}{2}$ and $\phi = \frac{3\pi}{4}$. In these regions there is more material present, so particles traversing them are more likely to interact. At $\phi = 0$ and $\phi = \pi$ another drop is visible. This is due to the fact that some of the read-out electronics are placed in the y-z-plane, impairing the detection there. The azimuthal angle distribution measured with pPB data is not perfectly described by the pp Monte-Carlo simulation. The origin of the discrepancy could not be found in the context of this thesis. The momentum distributions of the pPb data and the pp simulation, shown in figure 4.5c, have only small deviations. Figure 4.5d shows distributions of the impact parameter of all particles, prompt particles and secondary particles. They are determined using simulated events. By requiring tracks to have an impact-parameter $ip < 0.2$ mm, the portion of secondary particles is reduced. Secondary particles are expected to have higher impact parameters because they are produced in particle decays or interaction with detector material.

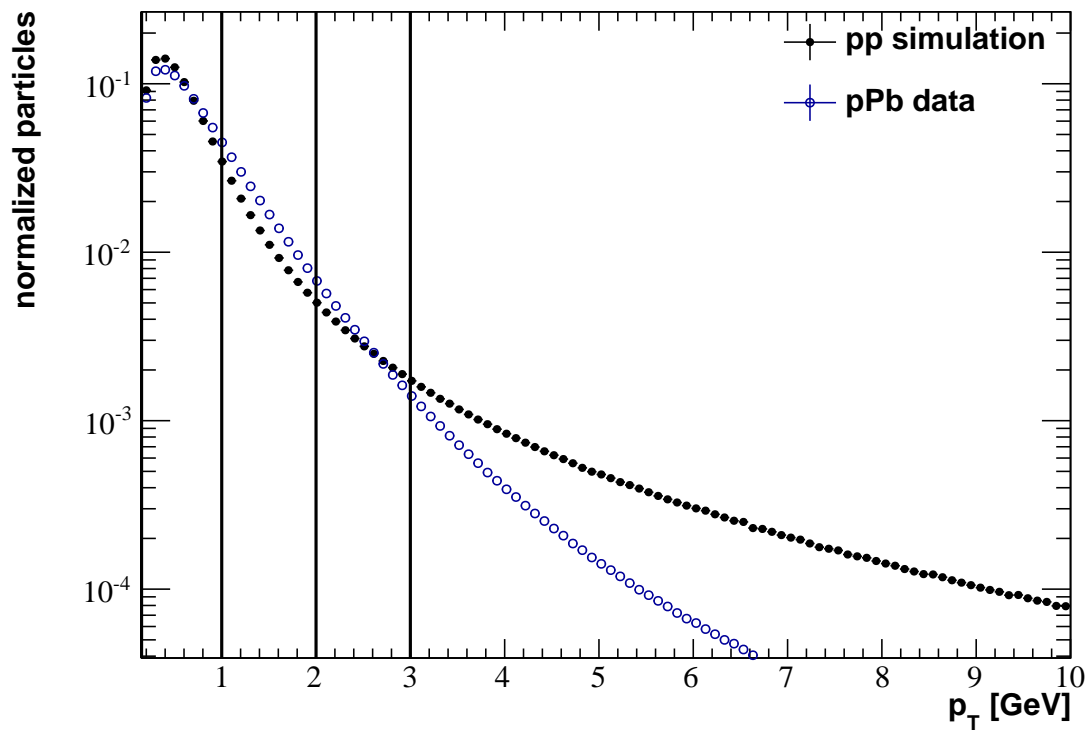
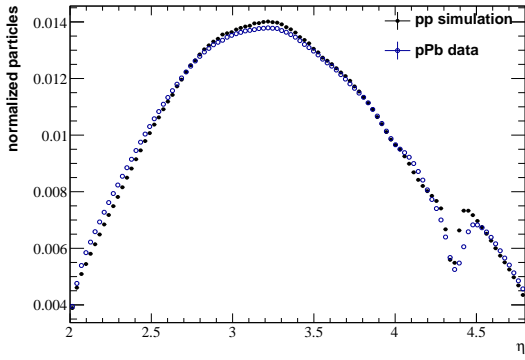
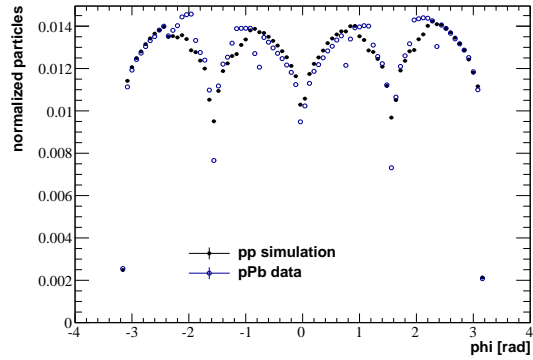


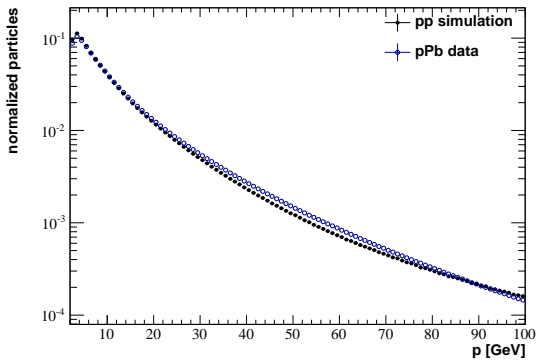
Figure 4.4: Transverse momentum distribution of pPb data and the pp simulation



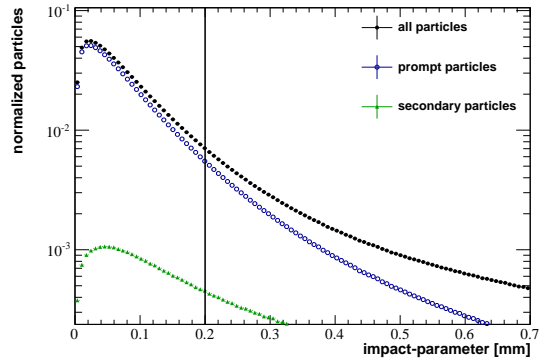
(a) pseudo-rapidity



(b) azimuthal angle



(c) momentum



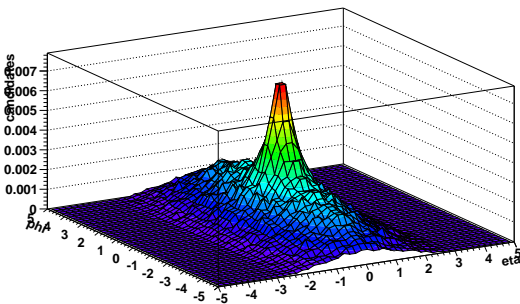
(d) impact-parameter for pp simulation

Figure 4.5: Kinematic properties of the selected tracks

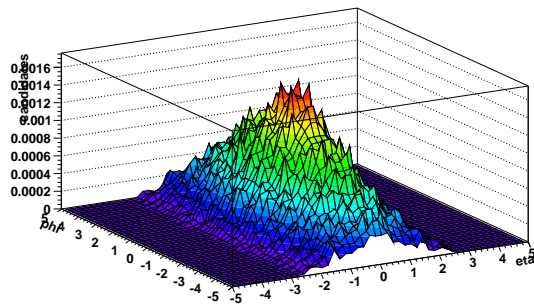
5 Determination of the two-particle angular correlation function

The first part of the analysis employs a method first proposed by the CMS-collaboration [15]. In order to calculate the correlation function of interest, a signal- and a background-distribution had to be constructed. The signal contains all present particle correlations, of which the correlations we are interested in can be isolated using the background.

The first step is to form two-particle-pairs for all possible combinations of particles within a single event. The angular differences of these pairs, $\Delta\eta = |\eta_1 - \eta_2|$ and $\Delta\phi = |\phi_1 - \phi_2|$, will be investigated. Pairs consisting of two times the same particle would solely yield values of $\Delta\eta = \Delta\phi = 0$, these pairs are excluded as they don't contain any useful information. This leads to $N(N - 1)$ pairs per event, where N denotes the number of selected particles in the event. The values $\Delta\eta$ and $\Delta\phi$ of every pair are taken to be positive and filled into a histogram. This is valid because their sign depends only on the order of subtraction and is not physically relevant. The distribution is then mirrored to the other three quadrants. Afterwards the entries per bin are divided by the number of



(a) signal



(b) background

Figure 5.1: Examples of signal- and background-distributions

selected particles in the event, so that the distribution represents a “per-particle signal distribution”:

$$S(\Delta\eta, \Delta\phi) = \frac{1}{N} \cdot \frac{d^2 N^{signal}}{d\Delta\eta d\Delta\phi} \quad (5.1)$$

Here N^{signal} is the the number of entries (in a certain $\Delta\eta$ and $\Delta\phi$ bin). The final signal is obtained by averaging over all events in the event class. Figure 5.1a shows an example of such a signal distribution. The increase of the signal towards smaller values of $\Delta\eta$ and $\Delta\phi$ is caused by particles produced in jets but it is also due to the fact, that the majority of the particles fly in a direction close to the beam axis, resulting in a high amount of small angular differences of the particle pairs. This effect is unrelated to any actual correlations and can be removed using a background-distribution, so that the much smaller particle correlations are visible. The contribution of a single event to the background is calculated by forming pairs consisting of particles from this event and a number of other events (mixing-events): The first particle in the event is selected and is paired up with all particles in all mixing-events. The angular differences of the pairs are filled into a histogram. This process is then repeated for all remaining particles in the event. As the detector-acceptance changes, depending on the z-position of the primary vertex, a cut on this variable is used. When selecting the mixing-events for a given event, the primary vertices may at most lie 2 cm apart in the z-direction. Lastly, a division by N yields the “per-particle background distribution”:

$$B(\Delta\eta, \Delta\phi) = \frac{1}{N} \cdot \frac{d^2 N^{background}}{d\Delta\eta d\Delta\phi}, \quad (5.2)$$

where $N^{background}$ is the number of entries due to mixed-event pairs. In the next step, the average background-distribution of all events is calculated. A comparison of both distributions in figure 5.1 shows that the steep increase towards $\Delta\eta = \Delta\phi = 0$ in the signal is also present in the background and therefore not related to any actual particle-correlations.

Using the background-distribution, we obtain the desired correlation-function:

$$C(\Delta\eta, \Delta\phi) = B(0, 0) \cdot \frac{S(\Delta\eta, \Delta\phi)}{B(\Delta\eta, \Delta\phi)} \quad (5.3)$$

Note, that one cannot simply divide the signal by the background, as the background-distribution depends on the amount of particle-pairs, which in turn is determined by the number of mixing-events. This means, using more mixing-events would result in a higher background and would therefore downsize the correlation-function. This is why we multiply the signal-to-background ratio by an additional factor, $B(0,0)$, the yield in the background-distribution at $\Delta\eta = \Delta\phi = 0$, which is bin with the highest value in the distribution. The result is a background with a yield of 1 at it's peak.

When constructing the signal- and background-distribution, particle pairs with $\Delta\eta < 0.02$ and $\Delta\phi < 0.02$ are omitted. This is done to reduce the amount of pairs stemming from a γ -conversion ($\gamma \rightarrow e^+e^-$). Figure 5.2 shows the opening angle in η and ϕ between the two electrons. This cut does as well remove pairs made up of clone-tracks. These tracks share mostly the same hits in the tracking system, but are considered as individual track candidates. Their angular distribution, which can be determined using the simulation, is shown in figure 5.3. The Angular differences of such a pair are typically much smaller than 0.02, so they are removed as well. The best way to treat clone tracks would be to only discard one of them, but as there are roughly thirty times as much electron-positron pairs as there are clones, it is reasonable to remove both particles in a pair. Lastly, the correlation function is calculated for three different classes of transverse momenta. This means that the signal and background distributions are constructed using only particles within a certain interval of transverse momentum. The multiplicity is determined using all selected tracks in the event.

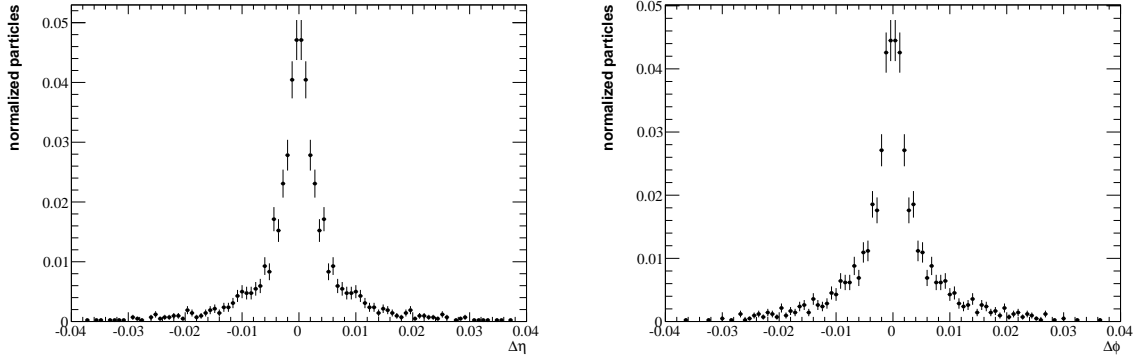


Figure 5.2: $\Delta\eta$ - and $\Delta\phi$ -distribution of the electrons produced in γ -conversions

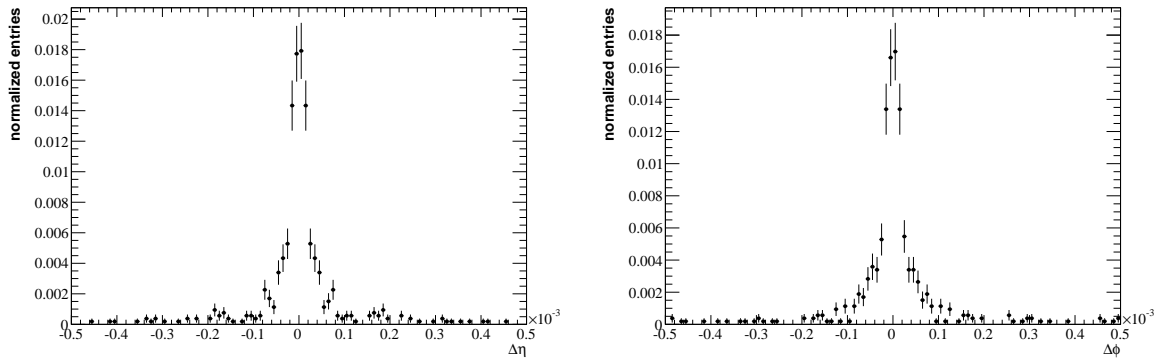


Figure 5.3: $\Delta\eta$ - and $\Delta\phi$ -distribution of clone-tracks

6 Corrections for tracking-efficiency, acceptance and ghostfraction

The corrections for tracking efficiency, acceptance and ghostfraction are determined using the Monte-Carlo simulation. The corrections applied to the reconstructed tracks are split up into three parts: tracking efficiency, detector acceptance and ghostfraction. Each of these contributes to the overall efficiency:

$$\epsilon = \frac{\epsilon_{tracking} \cdot \epsilon_{acceptance}}{(1 - ghostfraction)} \quad (6.1)$$

Each track is multiplied by the inverse of this factor. When filling the histograms, every pair is weighted by the product of both of its particles:

$$\epsilon_{pair} = \frac{1}{\epsilon_1 \cdot \epsilon_2} \quad (6.2)$$

6.1 Determination of the corrections

Tracking efficiency

The tracking efficiency is calculated by comparing all potentially reconstructible tracks to those that were in fact reconstructed:

$$\epsilon_{tracking}(\eta, p, vTracks) = \frac{\#reconstructed\ particles}{\#reconstructible\ particles} \quad (6.3)$$

$vTracks$ is the number of VELO-tracks. A track is reconstructible when it passes the kinematic cuts, belongs to a charged particle and has hits in the VELO and the main tracking stations.

The tracking efficiency is dependent on pseudo-rapidity η , momentum and the number of VELO-tracks in an event. Figure 6.1 shows the integrated efficiency as a function of η , p and the number of VELO-tracks, with indicated bins. The boundaries of the

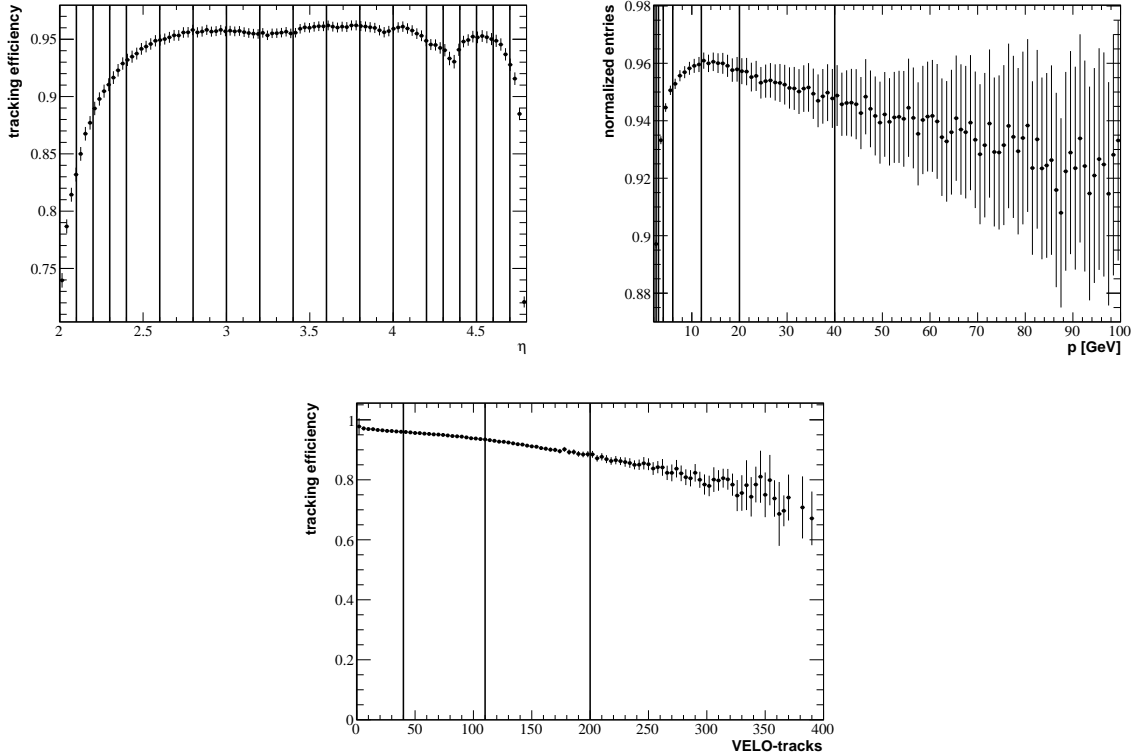


Figure 6.1: Tracking efficiency as a function of pseudo-rapidity, momentum and VELO-tracks.

bins were chosen such that the deviation from the mean within the bin was as small as possible, while maintaining a large enough number of entries to keep the statistical error small. The bins of VELO-tracks and momentum have to be wider at high numbers of tracks and momenta, because statistics rapidly decreases there. The two-dimensional tracking efficiencies can be seen in figure 6.2. In general the tracking efficiency is lower at the boundaries of the accessible range of pseudo-rapidity and at lower momenta. Furthermore the tracking efficiency decreases the more VELO-tracks are present, which is not unexpected, since the track finding efficiency depends on the multiplicity. Also visible is a region at high pseudo-rapidities and low momenta, where no reconstructible tracks are present. This is because tracks with these kinematic properties are outside the detector acceptance. The mean tracking efficiency is found to be $\epsilon_{tracking} = 0.93$.

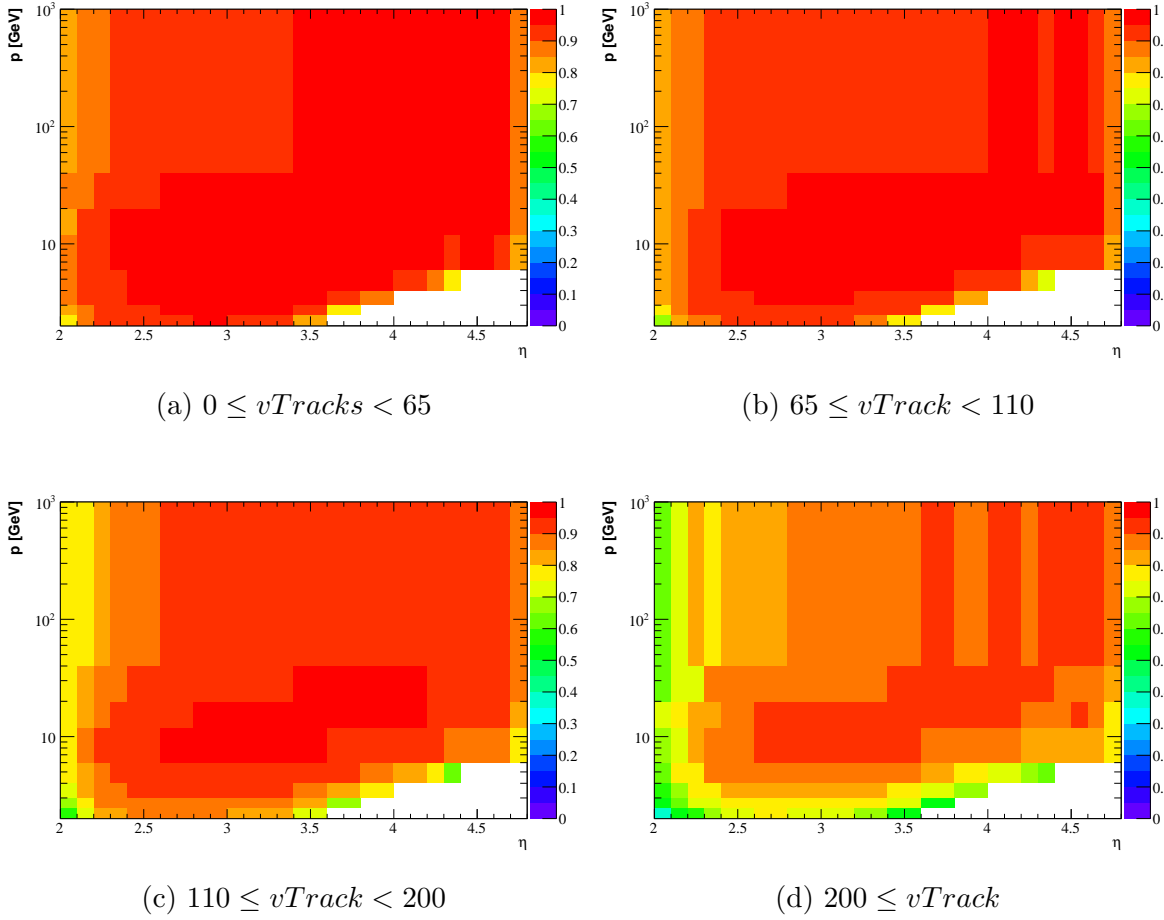


Figure 6.2: Tracking efficiencies

Acceptance

The acceptance is determined by the geometry of the detector and the magnetic field, which bends low momentum tracks out of the sensitive detector. It is defined by:

$$\epsilon_{acceptance} = \frac{\#reconstructible\ tracks}{\#detectable\ tracks} \quad (6.4)$$

Detectable particles are all particles that pass through the kinematic cuts, reconstructible tracks are the same as in the definition of the tracking efficiency. The acceptance as a function of momentum and pseudo-rapidity, with indicates bins, can be seen in figure 6.3. Note that the acceptance decreases significantly at $4.3 \leq \eta < 4.4$. This is due to the shape of the beam pipe. Particles traversing this region have to pass through more material and they are more likely to interact. Interaction in general can result in energy loss,

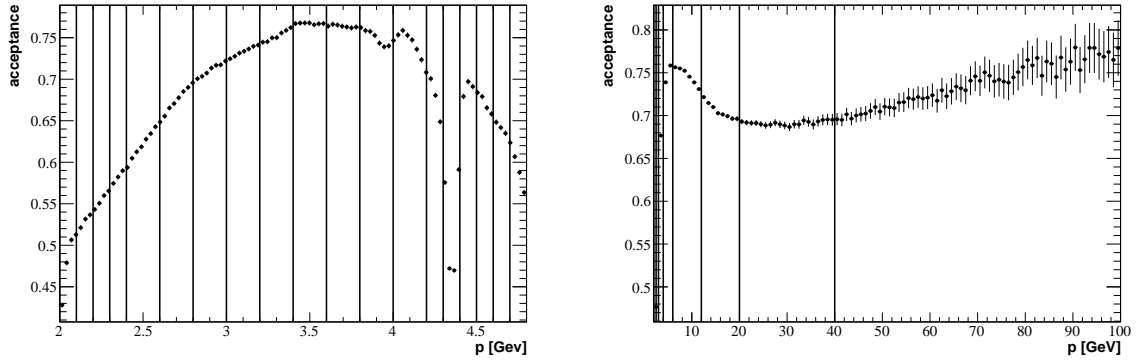


Figure 6.3: The left hand side shows the integrated acceptance as a function of pseudo-rapidity and momentum. On the right hand side the binning of the corresponding quantities is shown.

or in the form of scattering it may cause the particles to leave the detectors acceptance. The magnetic field forces particles with low momenta out of the detector, resulting in a lower acceptance at low momenta. The behaviour of the acceptance observed in the integrated functions can also be seen in the two-dimensional histogram in figure 6.4. The mean acceptance is found to be $\epsilon_{acceptance} = 0.72$.

Figure 6.5 shows the acceptances dependence on VELO-tracks and selected long tracks. The acceptance as a function of VELO-tracks looks as expected, it is constant over the whole range, except for a small increase at low VELO-track multiplicity. In contrast to this, the acceptance appears to be significantly lower for small numbers of selected long tracks. This behaviour was studied in the course of this thesis but could not be finally resolved. It seems to be the result of a correlation between the number of reconstructible tracks and selected long tracks for low multiplicity events. We therefore decided not to use any bins of multiplicity, when calculating the acceptance. ¹

¹The number of reconstructible tracks is closely correlated to the number of long tracks. An entry in the histogram at a low number of long tracks may come from an event with a high number of generator particles, of which only a few are reconstructible, leading to a low acceptance. This is not possible for events with high acceptances, because the acceptance can't exceed 1. The result is an acceptance function that is too low at low numbers of long tracks and that is too high at high numbers. Nonetheless this effect might not be strong enough to explain the drop at small numbers of selected tracks. This behaviour should also be visible for VELO-tracks and T-station hits, because these quantities are also related to the number of reconstructible tracks. In practice, the number of VELO-tracks at a given number of long tracks may vary over a broad range, as can be seen in

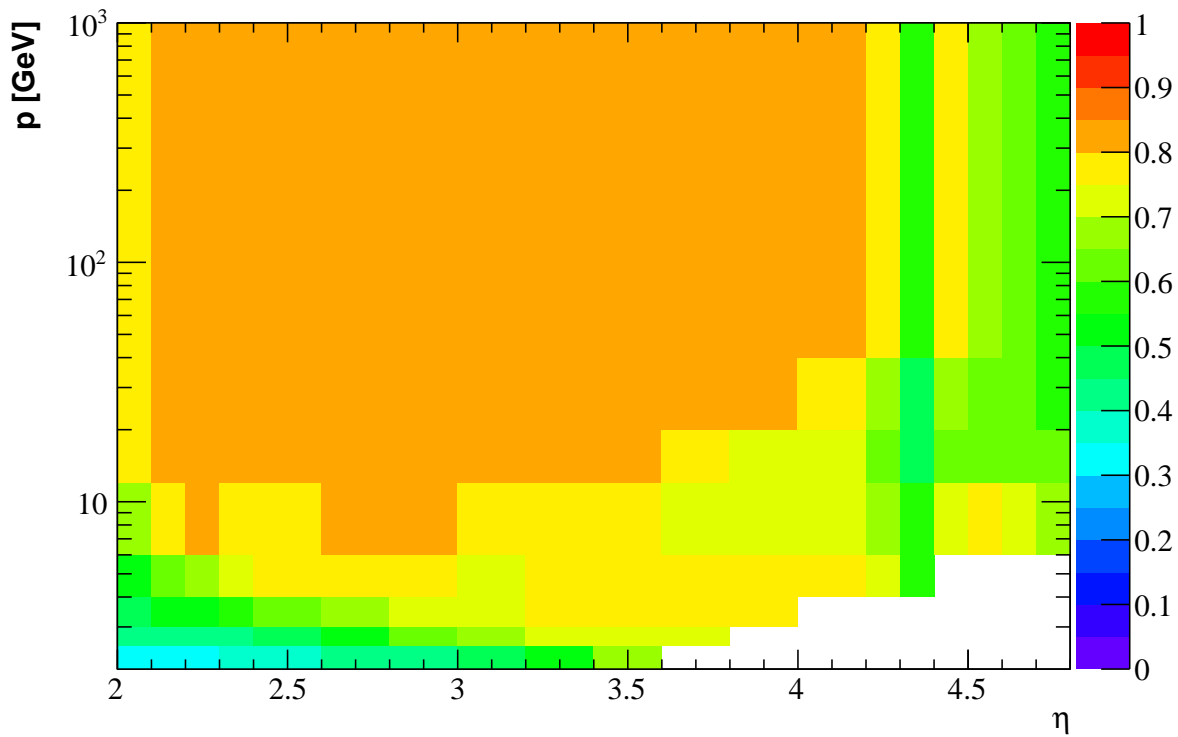


Figure 6.4: The acceptance as a function of momentum and pseudo-rapidity

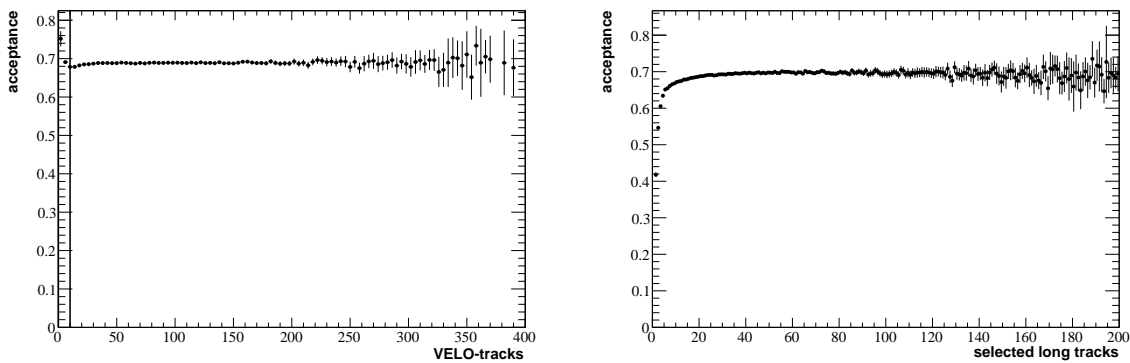


Figure 6.5: Integrated acceptance as function of VELO-tracks and selected long tracks

figure 6.6. This causes the acceptance (as a function of these quantities) to “smear-out”, so that it appears to be constant. When performing the corrections, using bins of selected tracks yields a better result. But as the acceptances behaviour concerning selected tracks cannot be simply transferred to pPb collisions, the acceptance is not binned, as suggested by the VELO-track dependency.

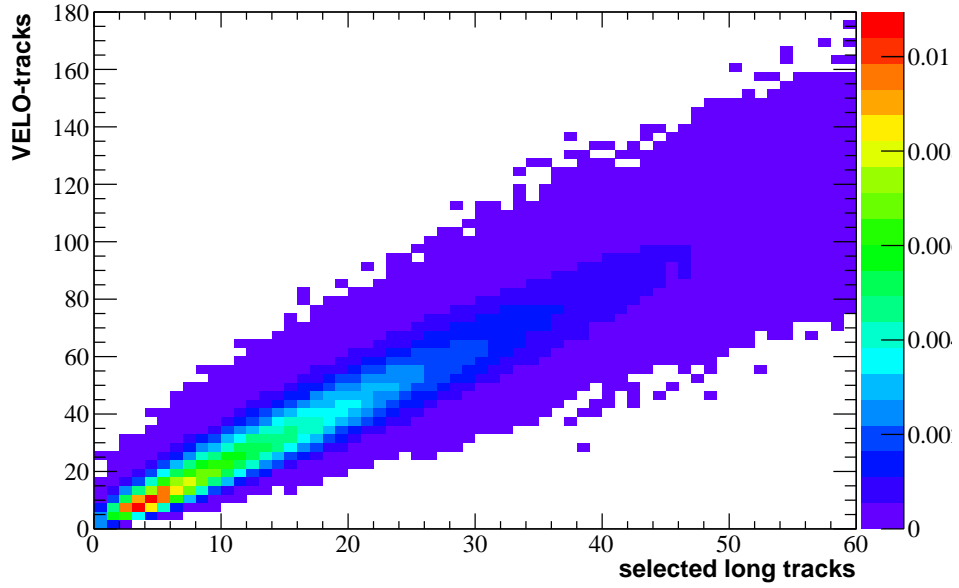


Figure 6.6: Correlation of VELO-Tracks and selected long tracks

Ghostfraction

In a simulated event, each track that is not a ghost track has an “associated particle”, which is one of the generated particles. By checking for these associated particles, ghost tracks can be found. The ghostfraction is therefore determined by comparing the number of reconstructed tracks, that pass the kinematic cuts, to the number of tracks without associated particles within this set:

$$R(\eta, p, vTracks, tHits) = \frac{\# \text{ reconstructed tracks not associated to mc. particle}}{\# \text{ reconstructed tracks}} \quad (6.5)$$

As figure 6.7 shows, the ghostfraction is dependent on pseudo-rapidity, momentum, the number of VELO-tracks ($vTracks$), and the number of T-station hits ($tHits$). The bin boundaries are indicated in figure 6.7. The bins have been chosen to keep the ghostfractions deviation small within them, while still maintaining high enough statistics. Because there are in total 16 histograms, only one example is shown in figure 6.8. The average correction for the ghostfraction is found to be $(1 - ghostfraction) = 0.89$.

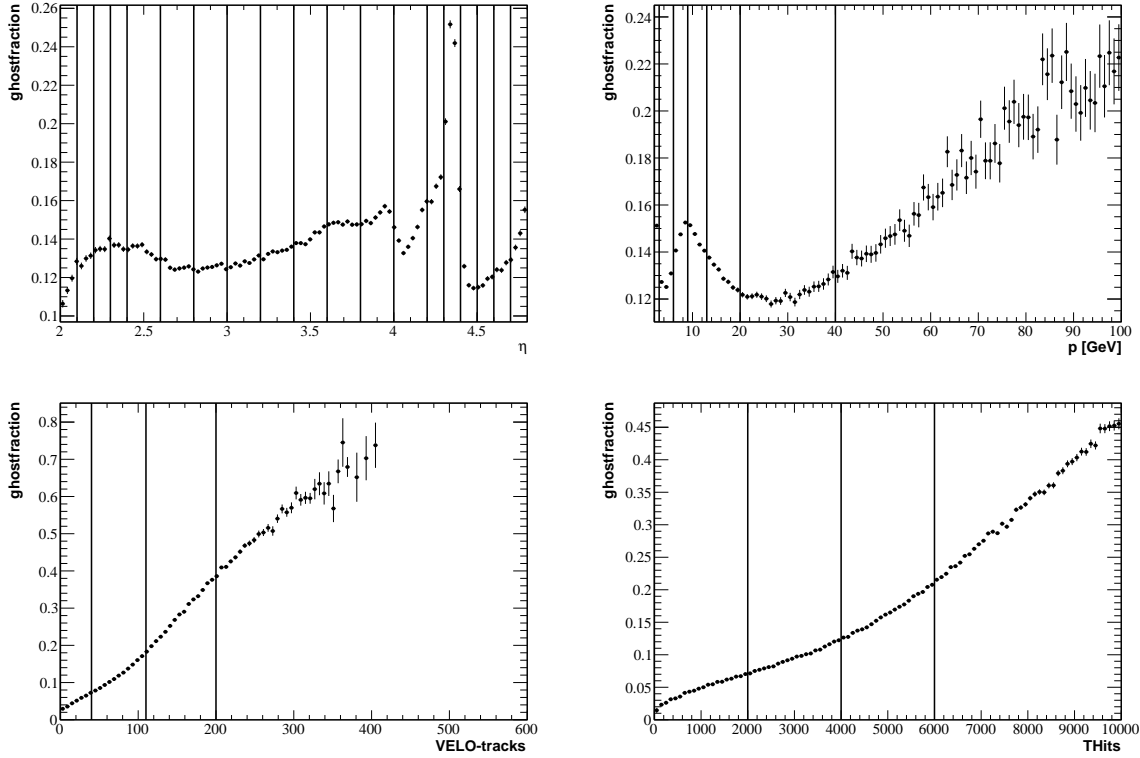


Figure 6.7: Integrated ghostfraction as functions of pseudo-rapidity, momentum, vTracks and tHits.

6.2 Consistency check and influence of binning

After calculating the acceptance, tracking efficiency and ghostfraction Tracking efficiency, acceptance and ghostfraction are all defined as a fraction of two sets of particles. The verification is done by iterating over the particles/tracks that have to be corrected in the nominator of the definition and weighting them with the appropriate efficiency. The sum of these weights has to match the true number of particles/tracks (in the denominator of the definition). These checks are performed separately as functions of pseudo-rapidity, momentum and the multiplicity. Furthermore, the pulls are calculated by dividing the difference between the true number of tracks (t) and the number of corrected reconstructed tracks (r) by the error of this difference:

$$c_{pull} = \frac{t - r}{\sqrt{(\Delta t)^2 + (\Delta r)^2}} \quad (6.6)$$

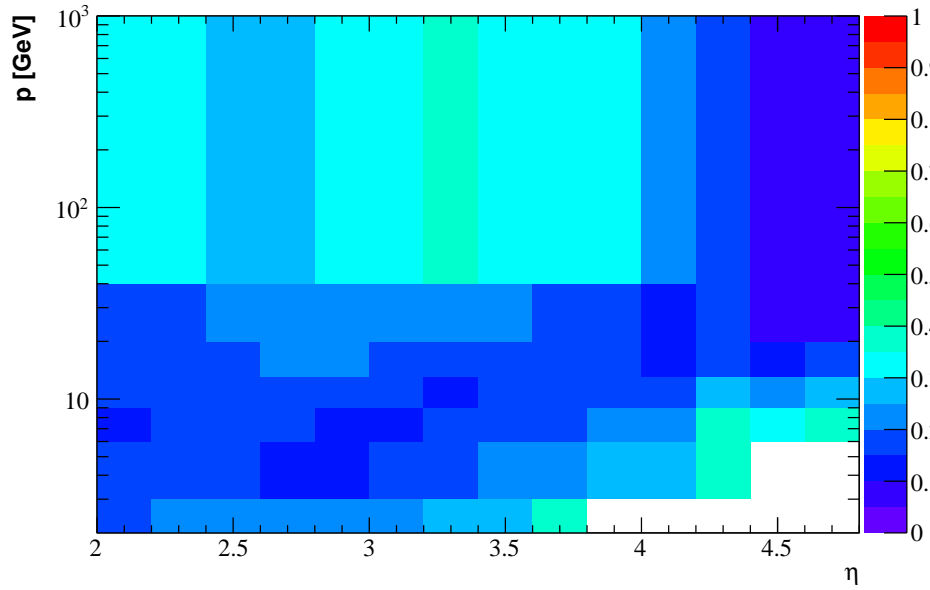


Figure 6.8: Ghostfraction for $40 \leq \text{VELO-tracks} < 110$ and $2000 \leq \text{T-station hits} < 4000$

Verification of the tracking efficiency

The tracking efficiency is determined in bins of pseudo-rapidity, momentum and the number of VELO-tracks. In the first step, the true number of particles is obtained by counting all prompt particles that pass the requirements described in section 4.2. In the second step, a subset is used, consisting of the particles which have been successfully reconstructed, weighted with the correction factor $\frac{1}{\epsilon_{\text{tracking}}}$ to account for inefficiencies. The results and their pull distributions are shown in figure 6.9. In case of the pseudo-rapidity, the pull distribution is close to zero, except for the lowest and the highest bins. Deviations there can be reduced by calculating the tracking efficiency in smaller bins. For this, a simulation containing more events would be needed, to have large enough statistics for a more precise three-dimensional binning. The influence of the binning is also visible in the pull distribution of the momentum, being close to zero except in the region $6 \text{ GeV} \leq p < 12 \text{ GeV}$. This region correspond exactly to one single bin of the calculated tracking efficiency. A single factor, the mean efficiency is used to weight all tracks within this regime, making the correction less precise for tracks with momenta further away from the mean momentum in the bin. The same effect can be observed in the pull distribution of the VELO-tracks, most notably at 40 VELO-tracks, where there

is a sudden change of approximately 2σ . This effect can be reduced by choosing smaller bins, but this would also require more simulated events.

Verification of the acceptance

The acceptance is investigated in the same way the tracking efficiency is verified. The true number of particles in this case is the number of generated prompt and charged particles, within the detectable region of pseudo-rapidity, momentum and transverse momentum. The second set of particles is the subset of these, meeting the additional requirement of intersecting the VELO and the main tracking stations. The verification is done separately for pseudo-rapidity and momentum, as is shown in figure 6.10. Both distributions show higher deviations, compared to the tracking efficiency. This is explained by the fact that the acceptance correction has on average a far bigger influence, than the tracking efficiency, so higher deviations are to be expected as well.

Verification of the ghostfraction

The verification of the corrections concerning the ghostfraction is performed by comparing the number of all reconstructed tracks to the number of reconstructed tracks, that are not ghosts-tracks, weighted with the factor $(1 - \textit{ghostfraction})$. Figure 6.11 shows that the correction becomes less precise around $4.2 \leq \eta < 4.4$, due to the influence of the beam pipe. Narrower bins in this region might improve the correction. In terms of momentum, the correction appears to be working properly. Regarding VELO-tracks and T-station hits, the pull distributions exhibit a clear structure. The same effect is also visible in the VELO-track dependency of the tracking efficiency correction, in figure 6.9 (bottom). The ghostfraction has been calculated in only four bins for both, VELO-tracks and T-station hits, due to the limited size of the data set.

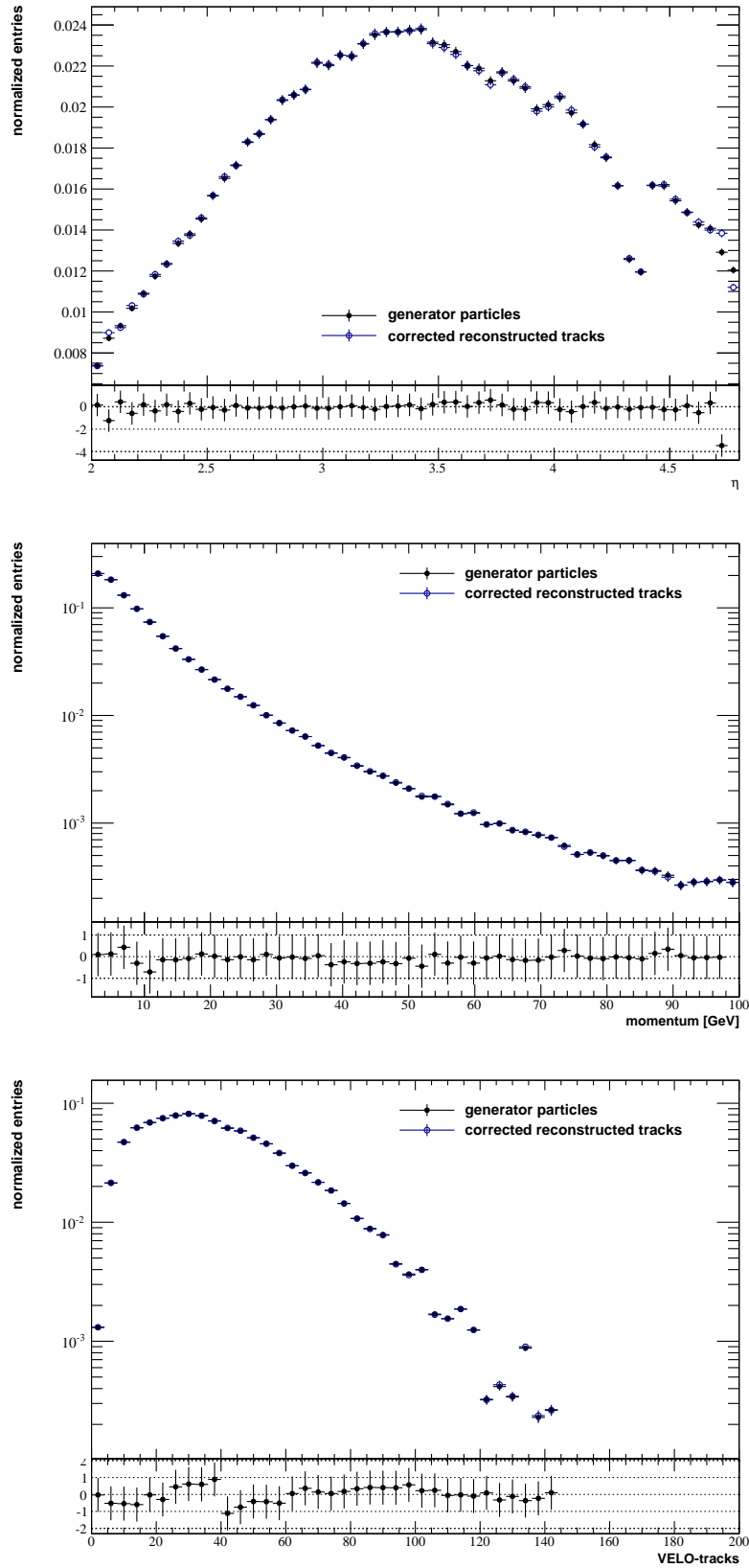


Figure 6.9: Corrections of the tracking efficiency as functions of pseudo-rapidity, momentum and VELO-tracks

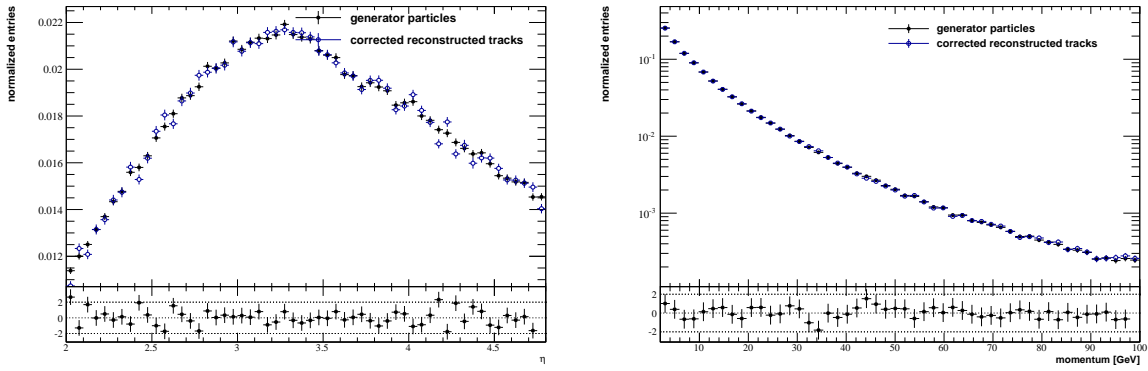


Figure 6.10: Corrections of the acceptance as functions of pseudo-rapidity and momentum

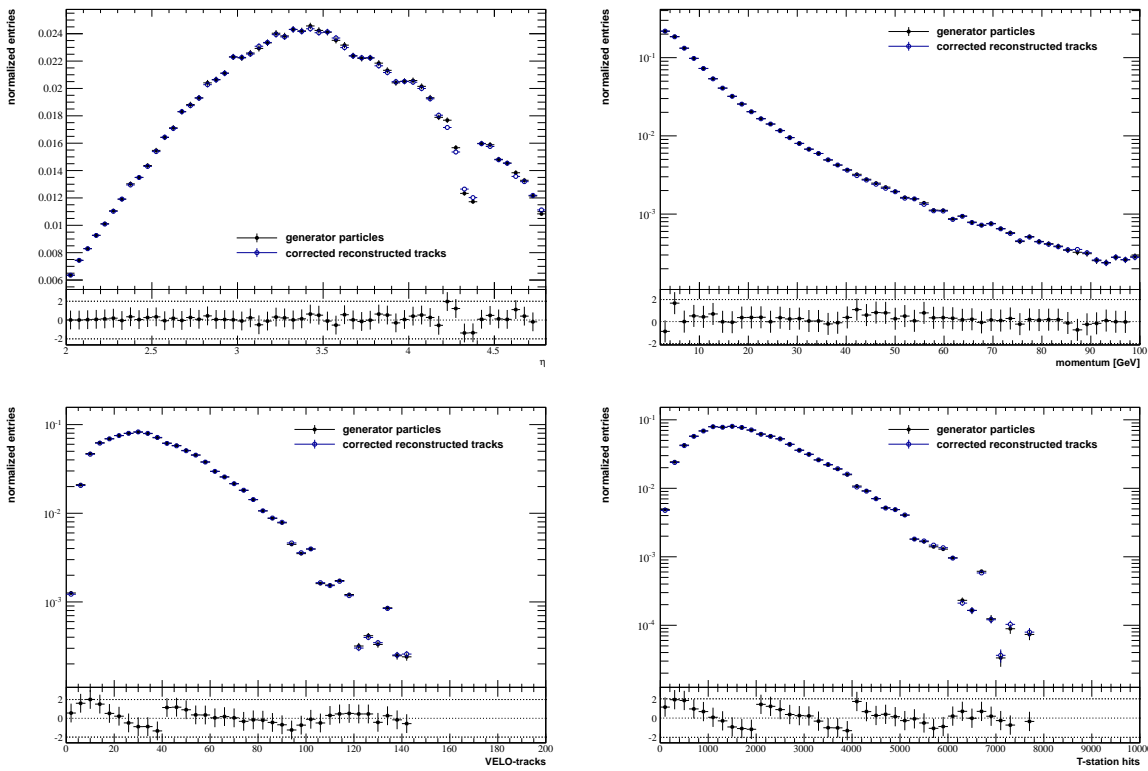


Figure 6.11: Corrections of the ghostfraction as functions of pseudo-rapidity, momentum, VELO-tracks and T-station hits

7 Results

Two-particle Correlation functions from different event classes are compared in figure 7.1. The $\Delta\phi$ range has been chosen so that all structures of the correlation function are visible. The most prominent feature in all of them is the near-side peak at $\Delta\eta = \Delta\phi = 0$, which has been truncated to be able to show the other structures. In the top left histogram, showing the angular correlations of particles from events with less than ten selected long tracks and $0.15 \text{ GeV} \leq p_T < 1.00 \text{ GeV}$, the near-side peak was not truncated, because of its low yield. This yield increases with multiplicity and the transverse momentum of the particles, because in both cases the contribution of jets increases. In the four leftmost histograms in figure 7.1 an expected ridge along $\Delta\eta = 0$ can be seen. It is most pronounced in the bin of lowest multiplicity and its yield gradually decreases with increasing multiplicity. Furthermore it also becomes less visible at higher transverse momenta, at $2.00 \text{ GeV} \leq p_T < 3.00 \text{ GeV}$ it cannot be distinguished, even in the bin of lowest multiplicity. This was expected, as it is caused by particles travelling in the forward region. In contrast, at low transverse momenta, the yield of the away-side ridge is small. In addition, its width and height increase towards large $\Delta\eta$. This effect vanishes at higher transverse momenta, a behaviour that is not yet understood. Most of the histograms seen in figure 7.1 show a shallow minimum at $\Delta\phi \approx 0$ and large $\Delta\eta$, caused by momentum conservation. At high multiplicities and transverse momenta, this minimum disappears and a ridge-like structure at $\Delta\phi = 0$ along η arises. It is visible in the histograms showing the correlation of particles from events with at least 40 selected long tracks, with the exception of the bottom left histogram. Particles with a low transverse momentum do not seem to contribute to this ridge like structure. The ridge-like structure most pronounced in the intermediate region $1.00 \text{ GeV} \leq p_T < 2.00 \text{ GeV}$ (see figure 7.2), although the difference to the bin of highest transverse momentum is small.

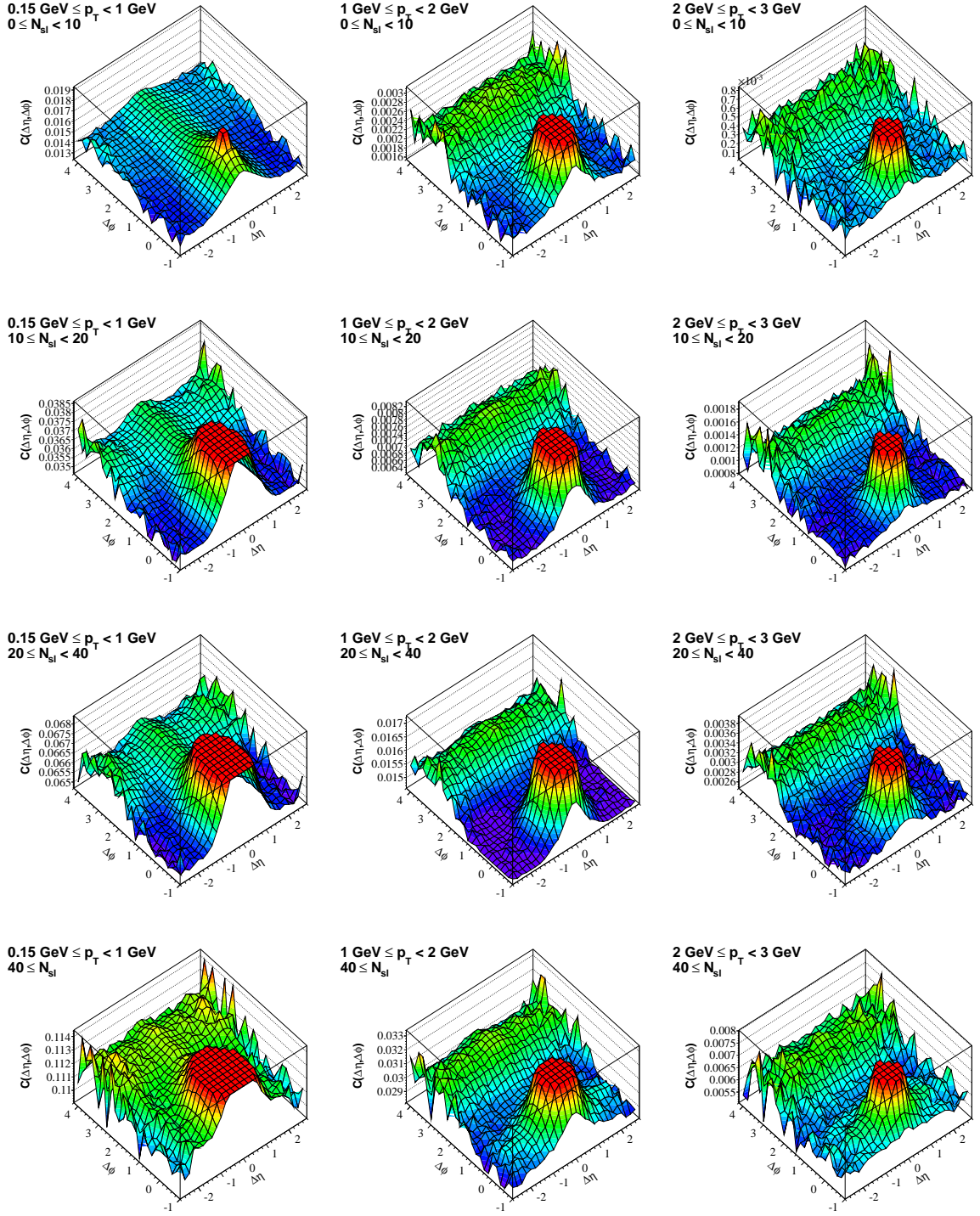


Figure 7.1: Two-particle angular correlation functions with truncated near-side peaks.

$1 \text{ GeV} \leq p_T < 2 \text{ GeV}$
 $40 \leq N_{sl}$

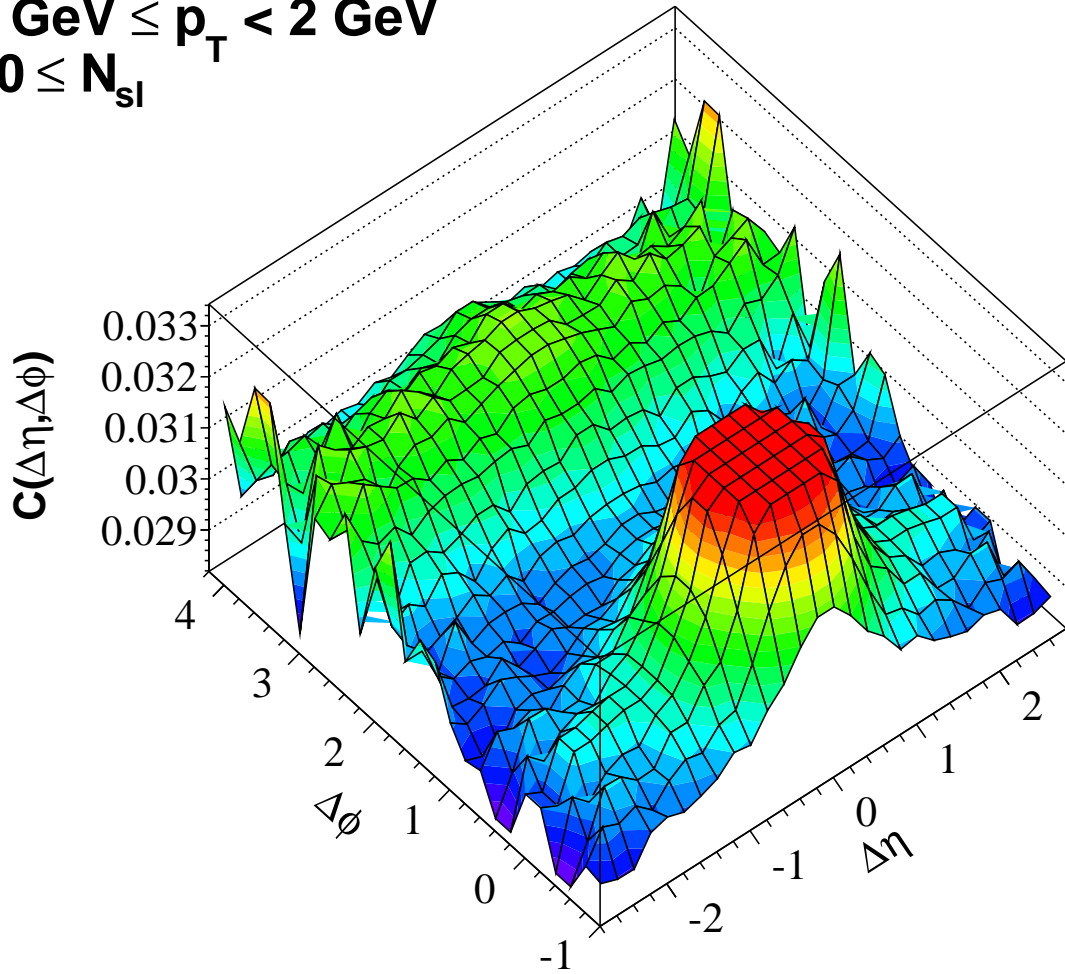


Figure 7.2: Two-particle angular correlations of particles from events with more than 40 selected long tracks and $1.00 \text{ GeV} \leq p_T < 2.00 \text{ GeV}$, where the ridge at $\Delta\phi = 0$, along $\Delta\eta$ is most pronounced.

To enhance the visibility of the near-side ridge and to better study the multiplicity dependence, figure 7.3 shows the projection of the two-dimensional distributions on the variable $\Delta\phi$, denoted by $C(\Delta\phi)$. For the projection, the region $|\Delta\eta| < 1.6$, that contains the near-side peak, is omitted.

In order to further investigate the multiplicity dependency of the ridge, calculation functions integrated over $\Delta\eta$ were obtained. Figure 7.3 shows these histograms in the four bins of multiplicity for $1.00 \text{ GeV} \leq p_T < 2.00 \text{ GeV}$. When integrating, the range $|\Delta\eta| < 1.6$ was omitted in order to suppress the yield of the near-side peak. Afterwards, a constant is subtracted from the values of all bins, to that the smallest value is zero. This shift is performed to facilitate the comparison, because the overall yield rises with increasing multiplicity, but only the relative size of the observed structures is of interest. In the bin of lowest multiplicity, the ridge is not present. Instead, only the away-side ridge is visible and $C(\Delta\phi)$ decreases towards $\Delta\phi = 0$. In the other three multiplicity bins, the ridge is visible. It reaches its highest yield in the bin of highest multiplicity, where it is approximately half the size of the away-side ridge.

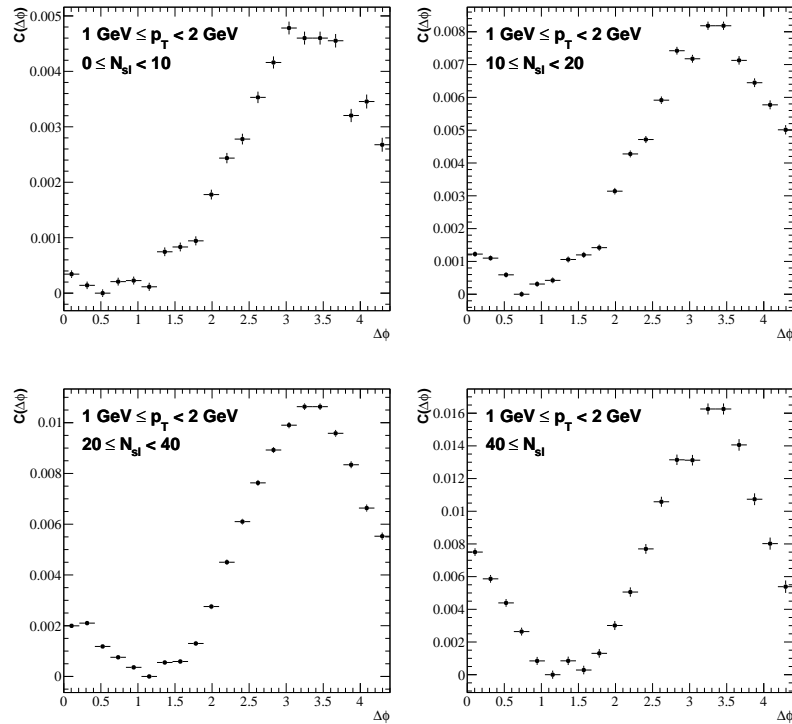


Figure 7.3: Two-particle angular correlation functions for $1.00 \text{ GeV} \leq p_T < 2.00 \text{ GeV}$ integrated over $\Delta\eta$

8 Conclusion

In this bachelor-thesis, two-particle angular correlations in proton-lead collisions have been investigated by using two-particle correlation functions. The main object was to verify the presence of a ridge-like structure in high multiplicity events, that has also been observed by experiments [15–17]. The analysis has shown that this structure is visible in kinematic forward region, covered by the LHCb detector. Its behaviour, depending on multiplicity and transverse momentum of the particles, is qualitatively similar to that, which has been reported by various other studies. Before a quantitative study can be conducted, the correction concerning detector effects have to be further studied. Their dependency on the number of selected tracks is not fully understood. A subject that would be worth a closer look, is the connection between the ridge at $\Delta\phi = 0$ and the away-side ridge. Recent studies by the ATLAS collaboration have hinted at a possible away-side equivalent of the ridge at $\Delta\phi = 0$ [21].

Bibliography

- [1] E. V. Shuryak “*On the Origin of the “Ridge” phenomenon induced by Jets in Heavy Ion Collisions*”, Phys. Rev. C76:047901, 2007.
- [2] C.-Y. Wong, “*The Momentum Kick Model Description of the Near-Side Ridge and Jet Quenching*”, Phys. Rev., C78:064905, 2008.
- [3] A. Dumitru, F. Gelis, L. McLerran, and R. Venugopalan, “*Glasma flux tubes and the near side ridge phenomenon at RHIC*”, Nucl. Phys., A810:91-108, 2008.
- [4] S. Gavin, L. McLerran, and G. Moschelli, “*Long Range Correlations and the Soft Ridge in Relativistic Nuclear Collisions*”, Phys. Rev., C79:051902, 2009.
- [5] Y. Hama, R. P. G. Andrade, F. Grassi, and W.-L. Qian, “*Trying to understand the ridge effect in hydrodynamic model*”, Nonlin. Phenom. Complex Syst., 12:466-470, 2009.
- [6] E. L. Berger, “*Rapidity Correlations at Fixed Multiplicity in Cluster Emission Models*”, Nucl. Phys. B85 (1975) 61.
- [7] A. Morel and G. Plaut, “*How Do Clusters Look in Semiinclusive Cross-Sections?*”, Nucl. Phys. B78 (1974) 541.
- [8] K. Eggert et al., “*Angular Correlations between the Charged Particles Produced in pp Collisions at ISR Energies*”, Nucl. Phys. B86 (1975) 201.
- [9] UA5 Collaboration, “*Charged Particle Correlations in $\bar{p}p$ Collisions at C.M. Energies of 200 GeV, 546 GeV and 900 GeV*”, Z. Phys. C37 (1988) 191
- [10] PHOBOS Collaboration, “*Cluster Properties from Two-Particle Angular Correlations in pp Collisions at $\sqrt{S_{NN}} = 200$ GeV and 410 GeV*”, Phys. Rev. C75 (2007) 054913

- [11] P. F. Kolb, P. Huovinen, U. W. Heinz et al., “*Elliptic Flow at SPS and RHIC: From Kinetic Transport to Hydrodynamics*”, Phys. Lett. B500 (2001) 232
- [12] B. B. Back et al., “*The PHOBOS Perspective on Discoveries at RHIC*”, Nucl. Phys. A757 (2005) 28
- [13] STAR Collaboration, “*Experimental and Theoretical Challenges in the Search for the Quark Gluon Plasma: The STAR Collaboration’s Critical Assessment of the Evidence from RHIC Collisions*”, Nucl. Phys. A757 (2005) 102
- [14] PHENIX Collaboration, “*Formation of Dense Partonic Matter in Relativistic Nucleus Nucleus Collisions at RHIC: Experimental Evaluation by the PHENIX Collaboration*”, Nucl. Phys. A757 (2005) 184
- [15] CMS Collaboration, “*Observation of Long-Range, Near-Side Angular Correlations in Proton-Proton Collisions at the LHC*”, arXiv:1210.5482v2 [nucl-ex], 22. Oct. 2012.
- [16] CMS Collaboration, “*Observation of Long-Range, Near-Side Angular Correlations in pPb Collisions at the LHC*”, arXiv:1210.5482v2 [nucl-ex], 22. Oct. 2012.
- [17] ALICE Collaboration, “*Long-Range Angular Correlations on the Near and Away Side in p-Pb Collisions at $\sqrt{s_{NN}} = 5.02$ TeV*”, Physics Letters B719 (2013) 29-41
- [18] ALICE Collaboration, “*Harmonic Decomposition of Two-Particle Angular Correlations in Pb-Pb Collisions at $\sqrt{s_{NN}} = 2.76$ TeV*”, arXiv:1109.2501v2 [nucl-ex], 24. Jan. 2012.
- [19] PHENIX Collaboration “*Dihadron azimuthal correlations in Au+Au collisions at $\sqrt{s_{NN}} = 200$ GeV*” Phys. Rev. C 78, 014901 (2008).
- [20] N. N. Ajitanand et al., “*Decomposition of harmonic and jet contributions to particle-pair correlations at ultrarelativistic energies*”, Phys. Rev. C 72, 011902(R) (2005)
- [21] ATLAS Collaboration, “*Observation of Associated Near-side and Away-side Long-range Correlations in $\sqrt{s_{NN}} = 5.02$ TeV Proton-Lead Collisions with the ATLAS Detector*”, Phys. Rev. Lett.

Erklärung

Ich versichere, dass ich diese Arbeit selbstständig verfasst und keine anderen als die angegebenen Quellen und Hilfsmittel benutzt habe.

Heidelberg, den 16.08.2013